Materialia 10 (2020) 100642

Contents lists available at ScienceDirect

Materialia

journal homepage: www.elsevier.com/locate/mtla

Full Length Article

The role of strain localization on the electrical behavior of flexible and stretchable screen printed silver inks on polymer substrates

Gabe Cahn[a], Alejandro Barrios[a], Samuel Graham[a], Jeff Meth[b], Antonia Antoniou[a,*], Olivier Pierron[a,*]

[a] G.W. Woodruff School of Mechanical Engineering, Georgia Institute of Technology, Atlanta, GA 30332-0405, USA
[b] Electronics and Imaging, DuPont Co., Wilmington, DE 19803-0336, USA

ARTICLE INFO

Keywords:
Screen printed silver inks
Flexible and stretchable electronics
Strain localization
Electrical resistance

ABSTRACT

This work explores conductivity under applied uniaxial strain of two silver-based inks with similar flake volume fractions of ~50% that are screen-printed with a single pass (thickness: 10 μm) onto three different polymer substrates. The normalized resistance increases more rapidly with applied strain for the "flexible" ink (5025 with an acrylic binder), and has three times greater resistance at 35% strain when compared to the "stretchable" ink (PE874 with polyurethane binder). While resistance increase is qualitatively consistent with percolation theory, the in-situ strain map analysis and post-mortem fractography reveal drastic differences in the root causes of the inks' electrical behavior. Both inks form strain localization bands with similar spacing. For the flexible ink (5025), strain localization is accompanied by local necking and flake fraction reduction. For the stretchable ink (PE874), strain localization is associated with surface cracking initiated by pre-existing voids, with minimal changes in the flake fraction. A model incorporating strain localization through a Gaussian distribution of flakes evolving with applied strain more closely accounts for the 5025 ink's normalized resistance increase compared to models that assume uniform strain and a uniform flake distribution. Overall, local necking and reduction of the flake fraction appear to be more detrimental to the resistance than the formation of surface cracks.

1. Introduction

Electronic devices are prevalent throughout personal and professional life activities; communication [1], health and environmental monitoring [2,3], energy capture [4] and storage [5] are only a few of the numerous applications in regular use. As these product markets evolve, and new ones emerge, so do desired uses extend beyond those for conventional rigid circuit boards. Many of the new devices must conform to nonplanar, organic surfaces, such as skin. Such applications require electronics to operate effectively after, and often during, exposure to high strain (for example, up to 30% for wearable applications). In short, they must be bendable, stretchable, and otherwise flexible, and researchers have increasingly risen to the challenge [6].

Several types of compliant conductors [7,8] are in development to satisfy strain requirements, each with mechanical limitations. Metals and carbon have shown promise when deposited as surface film coatings [9–11] onto, or embedded as nanowires or nanotubes [12–17] within, polymeric substrates to form conductive circuit traces. One drawback of thin metallic films is their substantial elastic property mismatch with the polymer substrate, often leading to early degradation of the electrical behavior due to cracking. Numerous studies have investigated the microstructural effects on onset of cracking in such films [18–28]. Conductive polymers are also useful as films [29–31], and have even been functionalized for actuation [32–34], but may irreversibly deform and de-bond when elongated. More complex architectures are formed when metallic interconnect structures, such as micropillar arrays [35], serpentine lines [36], and buckled films [37], are attached to elastomers, however they are similarly susceptible to irreversible elongation and delamination from substrates. Finally, hybrid conductors are created when conductive filler particles are added to a polymer binder [38–40]. At a certain filler volume fraction threshold, these independent particles form a cohesive percolation network, across which current can flow. When strained, the conductor volume will initially increase. This phenomenon is relatively isolated to the polymer matrix, resulting in a decrease of conductor volume fraction, which may result in a decrease in conductivity with potential breakdown of the percolation network. Consequently, hybrid conductors with polymer matrices having large Poisson's ratio, ν, around 0.5, are expected to electrically perform better under strain. The first motivation of this work is to experimentally check this effect by comparing two commercially-available hybrid

* Corresponding authors.
E-mail addresses: antonia.antoniou@me.gatech.edu (A. Antoniou), olivier.pierron@me.gatech.edu (O. Pierron).

https://doi.org/10.1016/j.mtla.2020.100642
Received 23 December 2019; Accepted 28 February 2020
Available online 2 March 2020

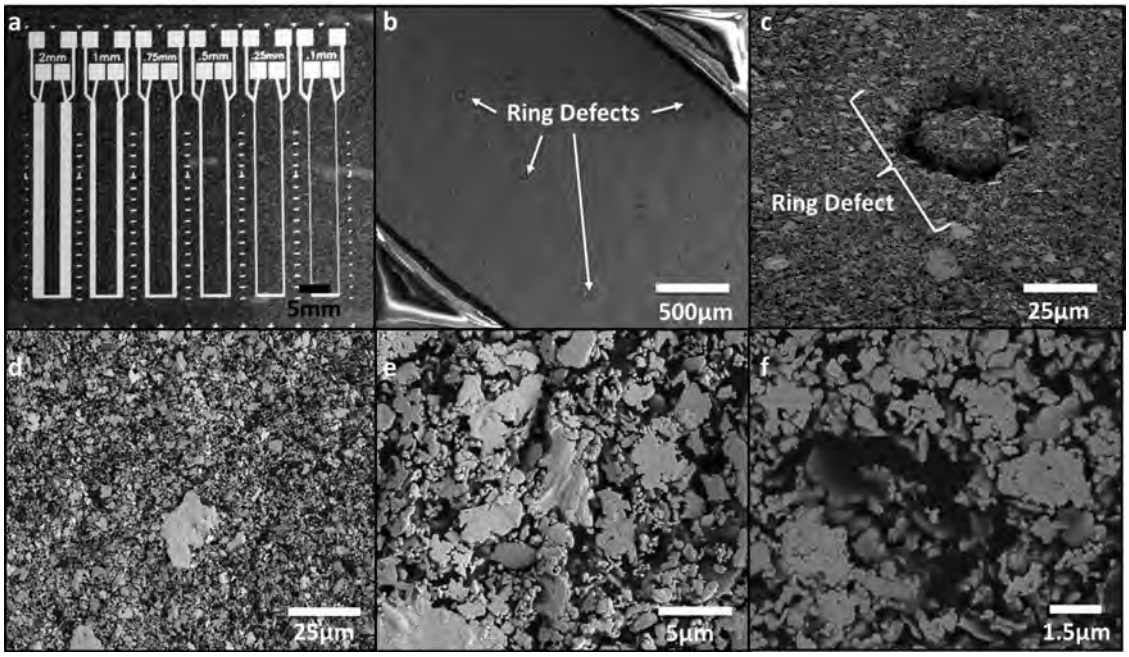

Fig. 1. (a) Optical image of the 5025 specimens showing sample design and trace width variations (b-f) Plan view SEM images of the unstrained ink surface. (b)–(c) Show ring like surface defects at two magnifications. (d)–(e) show the ink surface at different magnifications. The silver flakes appear randomly dispersed on the surface.

conductors whose main difference is the polymer binder (viscoplastic vs. elastomeric) having different Poisson's ratios, ν ($\nu \sim 0.35$ vs 0.48) and same silver flake type and volume fraction. Two screen-printed (nominal thickness: 10 µm) silver inks, with similar Ag flake volume fractions of ~50%, were investigated. The first ink (5025) has flakes embedded in an acrylic binder ($\nu \sim 0.35$), while the second ink (PE874) consists of flakes embedded in a polyurethane binder ($\nu \sim 0.48$). The choice of the binder is related to the type of substrate on which the inks are intended to be attached and the overall targeted applications (flexible vs. stretchable/wearable electronics): 5025 is a "flexible" ink and PE 874 is a "stretchable" ink.

First order approximations and models [41] are used to predict electrical performance in hybrid conductors. They assume uniform distribution of filler material, as well as uniform deformation. These models agree with experimental data for low applied strain [40,42], but not at large strains when non-uniform deformation is expected to occur. Therefore, the second motivation of this work is to investigate the behavior of hybrid conductors at larger applied strains (up to 35%). To do so, this work employed an in-situ^2 testing approach [43], whereby resistance measurements are taken throughout sample straining, while optical images of ink surfaces are simultaneously captured at regular intervals. In-plane strain maps are obtained from the surface images. Post-mortem Focused Ion Beam (FIB) cross sections observed under the Scanning Electron Microscope (SEM) are created to further understand the local architecture evolution due to straining and its role on resistance evolution. Overall, this investigation highlights that understanding the origin of strain localization is key to developing models capable of predicting the inks' electrical behavior under large strains.

2. Methods

2.1. Specimen geometry and ink properties

In this work, 5025 and PE874 inks from DuPont were separately screen printed onto polyethylene terephthalate (PET), Kapton® polyimide (PI), and thermoplastic polyurethane (TPU) substrates. The printing was performed at the DuPont Applications Laboratory with tightly controlled proprietary processes that have been optimized over years for the different inks and substrates. Substrate thicknesses were 127 µm for PET and PI, and 89 µm for TPU. A single pass screen print of these inks yields a nominal thickness of approximately 8–10 µm. The inks are then cured at 130°C for 15 min. Fig. 1 includes an optical image of 6 specimens printed onto PET with 5025 ink of varying widths from 0.1 to 2 mm (only the 2mm trace width specimens were used in this study). The specimens also include tick marks spaced 2 mm apart for spatial reference and test pads for 4-point resistance measurement.

5025 ink is composed of silver flakes embedded in a polymer matrix with an acrylic binder. The reported flake density is 50% by volume. PE874 contains the same volume fraction of silver flakes, but differs from 5025 by employing a polyurethane binder. Fig. 1(b)–(f) shows SEM images of the inks' surfaces at increasing magnifications. Qualitatively, the surfaces demonstrated no distinguishing physical characteristics in the unstrained condition. Ring-like defects (see Fig. 1(b) and (c)) are attributed to the printing process, and are likely artifacts of emulsion bubbles popping. Flake dimensions qualitatively range from hundreds of nanometers to tens of microns, with no obvious arrangements or concentrations.

The Young's modulus of 5025 is estimated to be 5 GPa, and that of PE874 is 1.5 GPa. PE874 is intended to be printed upon TPU substrates, with modulus on the order of MPa, while 5025 is considered more appropriate for PET and PI, whose moduli were measured to be approximately 2.5 and 3.5 GPa, respectively. This is to reduce modulus mismatch between substrate and film. Similarly, Poisson ratios of the hybrid inks are estimated to be 0.35 for 5025, and 0.48 for PE874. Published sheet resistivity values are between 12 and 15mΩ/sq/25µm for 5025, and <75mΩ/sq/25µm for PE874.

2.2. In-situ^2 setup

Uniaxial tension tests were conducted on a Linkam Scientific TST350 Microtensile Test Stage. This setup is designed for use in conjunction with both standard and transmission optical microscopes. Position resolution in this system is 10 µm (corresponding to a resolution of 0.03% in strain) [44]. Fig. 2 depicts a sample in the stage under

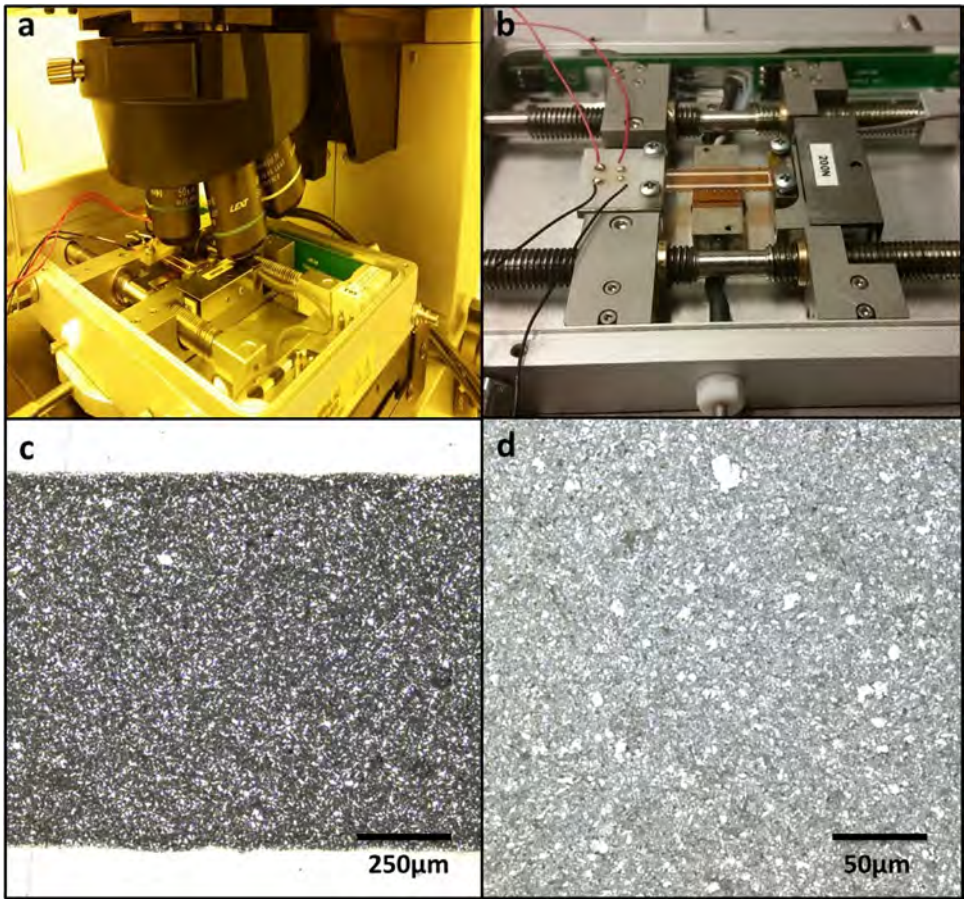

Fig. 2. Test fixturing and in-situ images: (a) Microtensile stage under confocal microscope (b) sample loaded in microtensile stage with custom 4-point resistance measurement clamp (c) 1mm wide 5025 ink trace on PET (d) magnified 5025 ink surface.

a microscope. Custom clamps were designed such that the one end contains four spring loaded contacts attached to electrical leads (see Fig. 2(b)). As the clamps are tightened, contact is made with the four pads of the sample, with minimal depression. Leads coming off of the pads connect to an Agilent 34401a digital multimeter for in-situ resistance measurement. To eliminate slippage of high modulus substrates when loaded, the samples were attached to the clamps using commercial adhesives, either glue or double sided tape. Testing and data collection was handled through Labview, which allowed for proper time syncing of load and displacement measurements from the tensile test stage with resistance measurements from the multimeter. The sampling rate for data collection was approximately 2Hz. All strain experiments were performed using an applied strain rate of 50 µm/s. Experiments were halted when measured resistance values became unstable, varying erratically, indicative of an open circuit within the ink, or when the load values in the sample approached the 200 N limit of the test stage.

Optical images were taken periodically using an Olympus LEXT 4100 confocal microscope, which is capable of both optical imaging, as well as laser profilometry. The surface roughness of these inks was on the order of 1µm RMS, with peak and valley disparities of several microns, well beyond the depth of field of standard optical scopes. This equipment takes incremental height scans, and uses software to stitch them into a cohesive image. Images were sampled at specified values of strain, whereby the test was halted for durations of no more than 3 minutes to allow the microscope to complete its scans under static conditions. Fig. 2(c) and (d) shows 5025 ink sample images taken at 10× and 50× magnification, with spatial resolutions of 1.25 µm/pixel and 0.25 µm/pixel, respectively. These image sets were later used for in-plane strain map analysis.

2.3. In-plane strain maps

High magnification optical images were taken in-situ at regular increments of strain. These image sets were then processed using an open source digital image correlation software, Ncorr, created at Georgia Tech [45]. Plane view images of the ink samples in the unstrained condition were used as reference images. The flakes and matrix forced a natural contrast that was used to track the local displacement field. Ncorr, like other subset-based DIC algorithms, divides a patterned image into smaller areas (subsets) and monitors their movement in subsequent images that are obtained during deformation, e.g. uniaxial stretching of the inks.

The analysis provides in-plane displacements u and v with sub-pixel resolution for each subset center, since deformation in each subset is assumed to be a linear, first order transformation. Both the subset radius, r_s, as well as the subset overlap can be varied. Ncorr obtains in-plane strains from the gradients of a least-square plane fit over a group of subset center points of size w_e from the displacement field.

The DIC parameters, r_s and w_e, were determined from a Rigid Body Translation (RBT) analysis of two reference images of each ink. The reference images were taken prior to each strain test, whereby the translated image was obtained by shifting the sample stage beneath the scope lens by a few millimeters in a single direction. Any deviation from zero (no strain) in the resulting Ncorr analysis will give the uncertainty in the measured displacement or strain under uniform stretch of a given pattern. This error was calculated for different values of the subset radius and strain window with the minimum substep overlap of 1 pixel, providing a low bound estimate of the error in the strain field assuming that the deformation is uniform. Based on the above evaluation, subset radii of 10 pixels and strain radii of 5 pixels were selected for all subsequent analysis. Given the optical image resolution of 4 pixels per micron, this

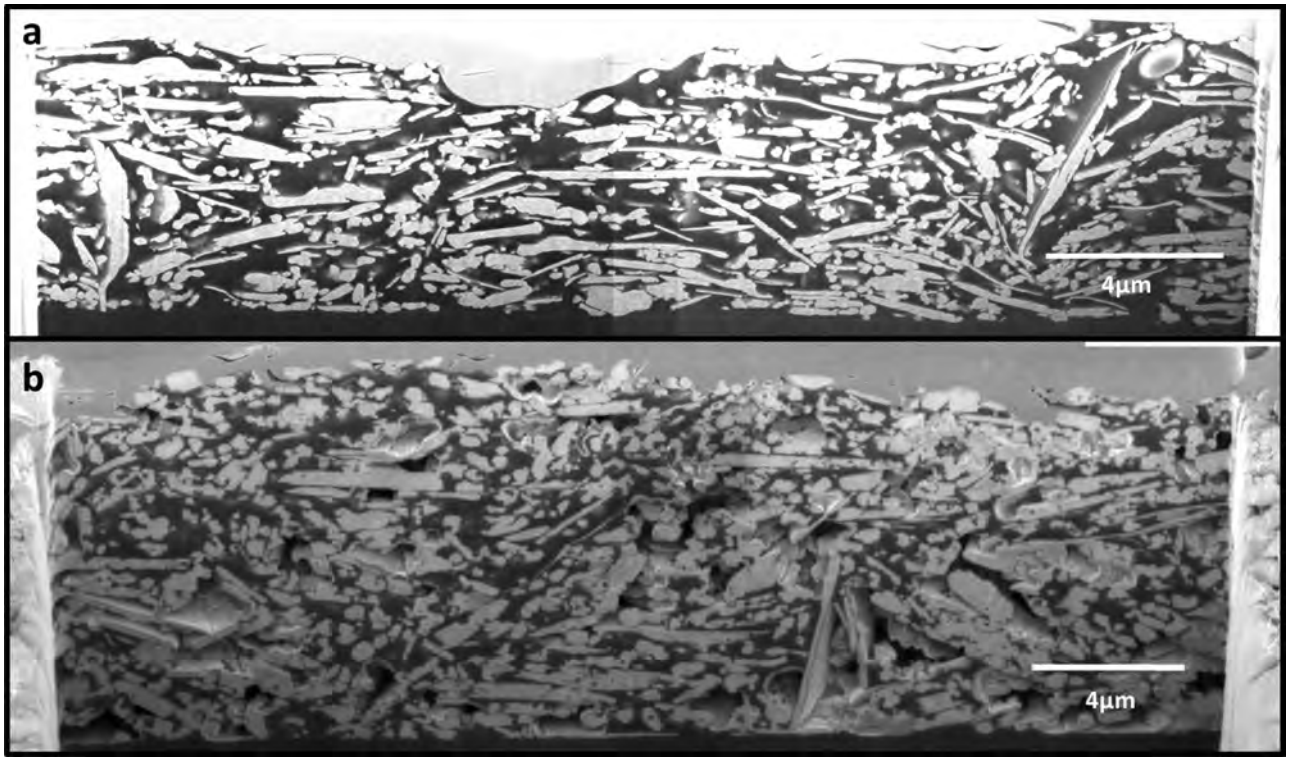

Fig. 3. SEM cross sections of both inks, taken at 52° tilt: (a) 5025 flexible ink, unstrained (b) PE 874 stretchable ink with voids, unstrained. The silver flakes appear light gray in color while the binder is darker gray. Voids are apparent in PE874 as darker (nearly black) areas.

translates to subset and strain windows sizes of 5 sq. μm and 2.5 sq. μm, respectively. The above subset window radius and strain window gave an error of 0.5% for the 5025 and 1.2% for PE874 in the direction of sample elongation.

2.4. Fractography

In order to quantify and understand the effect of straining on the inks' architecture (and especially the flake fraction), cross sections of specimens before and after mechanical testing were obtained using a focused ion beam (FIB) FEI Nanolab 200. Gallium ions were used to mill rectangular regions of the ink so as to expose the through thickness ink morphology e.g. height, flake fraction, etc. Platinum deposits of 1-2 μm were placed in cut areas ahead of time to preserve surface integrity. Post experiment cross sectioning also took place for comparative analysis. FIB cuts were initially made at 30 kV and 3 nA, followed by a polishing section cut at 0.3 nA to remove any atomized material that may have deposited onto the section surface during milling at higher current. After sectioning, samples were rotated 52° for SEM imaging. Thickness measurements were corrected for this angle.

Once captured, through thickness SEM images were used to identify characteristics of each ink before and after straining. This included ink thickness and area fraction of conductive filler. Using ImageJ [46], a Java-based image processing tool, screen shot images were converted to 8-bit data files. The images were binarized and statistics of the flake area fraction and local ink height were obtained along the width of the ~30 μm wide FIB sections.

3. Results

3.1. Initial characterization

Fig. 3 compares the respective cross sections of undeformed 5025 and PE874. In both inks we can see high dispersal of silver flakes, comparable to that of their surfaces. Flakes are observed to vary significantly in dimension, from several μm to hundreds of nm long. Qualitatively, a large proportion of long flakes, those measuring several μm, are oriented horizontally in line with the print direction. This is potentially due to shearing forces imposed during the screen printing process, and orientation that can occur during the drying process. It is also important to note that this cross-sectioning reveals inherent defects (voids) within PE874 that are not found in 5025. A possible reason for the presence of voids is the higher flake fraction for PE874 versus 5025 (54.5 vs 49%, respectively; see below). When the flake fraction is greater than the maximum packing fraction for random, loose packing (akin to the tap density), estimated to be 53%, voids may be created within a coating due to the porosity of polymer. The flakes do not pack down densely during drying, and air is subsequently incorporated into the coating.

The average initial thickness for 5025 is 9.1 μm, with standard deviation of 0.75 μm, while it is 11.8 μm for PE874, with standard deviation of 1.1μm. Given these thicknesses, a sample ink trace width of 2 mm, trace length 72 mm, the resistance is predicted using:

$$R = \rho \times \frac{L}{A} \tag{1}$$

where ρ is the resistivity, L length, and A cross section area. Given the sheet resistivity values reported in 2.1, the predicted resistance values are between 1.2 and 1.5 Ω for the 5025 samples, and less than 5.7 Ω for the PE874 samples. Average measured resistances are 2.2 Ω with standard deviation of 0.17 Ω for 5025 and 2.8 Ω with standard deviation of 0.47 Ω for PE874. The higher measured resistance in 5025 suggests that thickness measurement taken from the cross-section cut does not reflect the average value within the ink given the variability in thickness (several microns) observed from surface roughness measurements.

The initial FIB cross sections were used to calculate flake fraction distributions. Applying a normal distribution to flake fraction values over the entire cross section, 5025 presents a mean flake fraction of 49%, with standard deviation of 9%. Mean flake fraction in PE874 is higher, at 54.5% with standard deviation of 10%. The average void fraction is 17% for PE874; these voids vary in size, orientation, and aspect ratio.

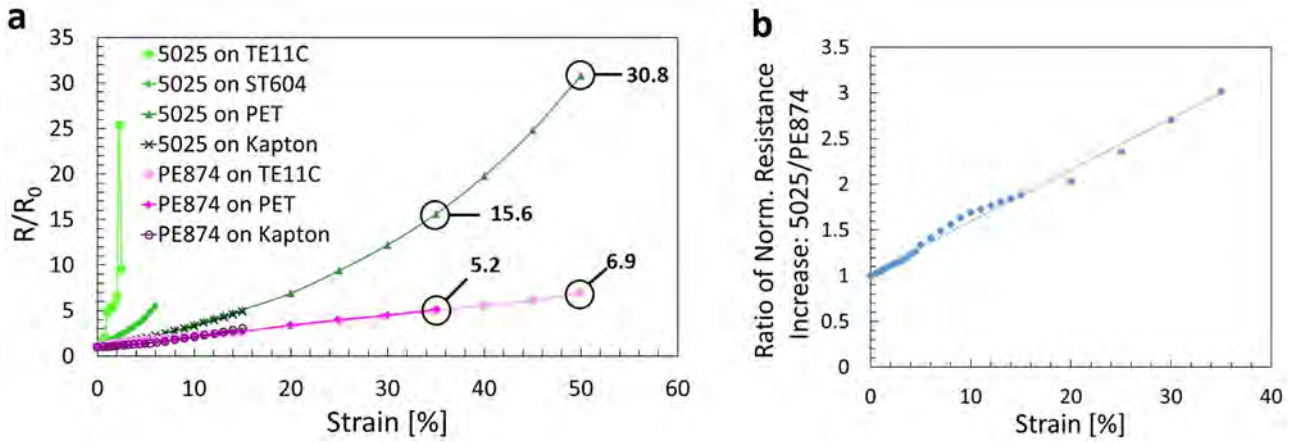

Fig. 4. (a) Normalized resistance with applied strain for the two Ag inks screen printed on different substrates (b) Ratio of relative resistance increase with strain between 5025 and PE874 printed onto PET.

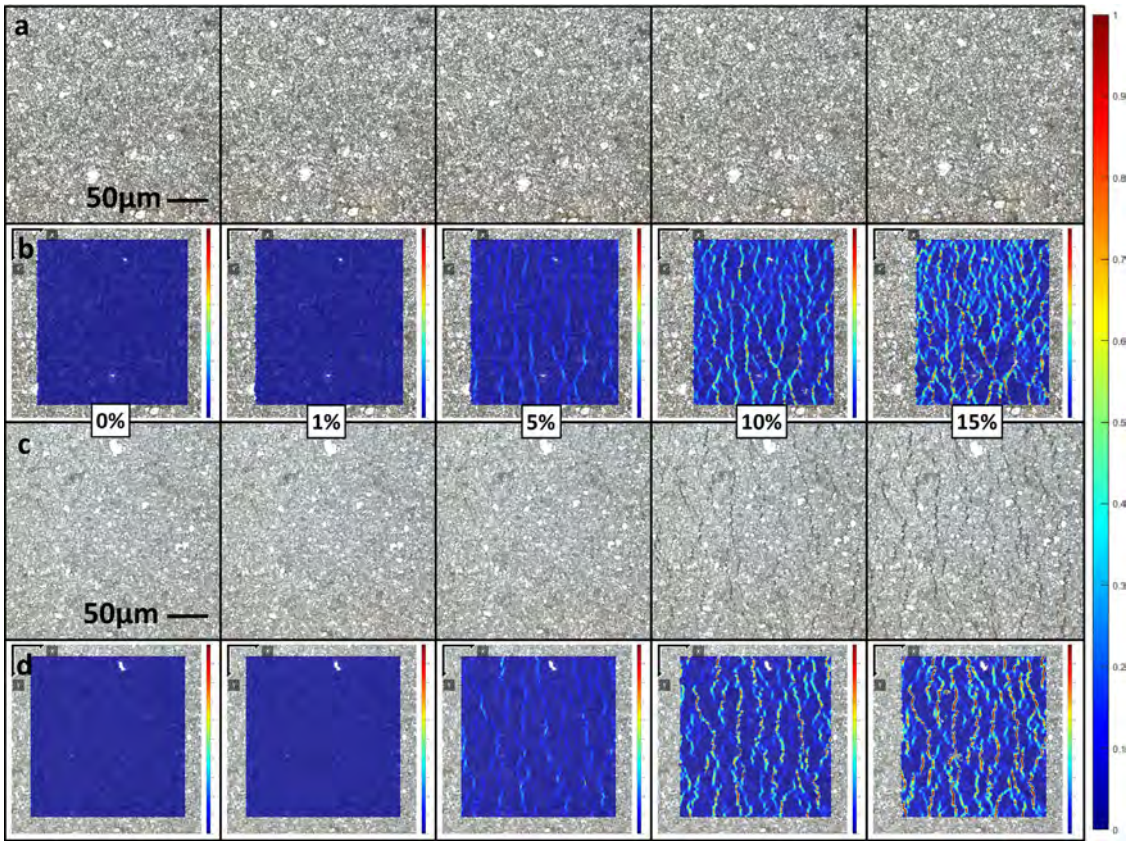

Fig. 5. Optical imaging and in-plane strain (ε_{xx}) for 5025 and PE874 under applied uniaxial far field strain values of 0%, 1%, 5%, 10%, and 15%. (a) 5025 flexible ink optical surface images. (b) 5025 strain field overlay. (c) PE874 stretchable ink optical surface images. (d) PE874 strain field overlay.

The smallest measure roughly 0.5 µm in diameter. Larger voids are as long as 6 µm, but are extremely narrow, measuring only about 0.3 µm across.

3.2. Normalized resistance vs. strain

The resistance in both flexible and stretchable inks increases with applied strain. As the initial unstrained resistance value is different between samples, the resistance values measured under strain are normalized with the undeformed resistance value. Fig. 4(a) shows the normalized resistance with applied strain for both inks onto the three different substrates. The normalized resistance of the flexible ink has a similar evolution when printed on PET and PI, but for the TPU substrates (TE11C and ST604) the normalized resistance increased at much higher rates. This is expected, given that 5025 is not meant to be used with TPU, due to large elastic modulus mismatch inducing cracking. The stretchable ink (PE874) did not exhibit a sensitivity to the substrate upon which it was printed, as all of its performance plots closely overlapped. These data highlight the importance of substrate on the electrical behavior under strain, especially for stiff inks on soft substrates. The rest of this paper focuses on data obtained on PET substrates, in order to compare the ink behavior.

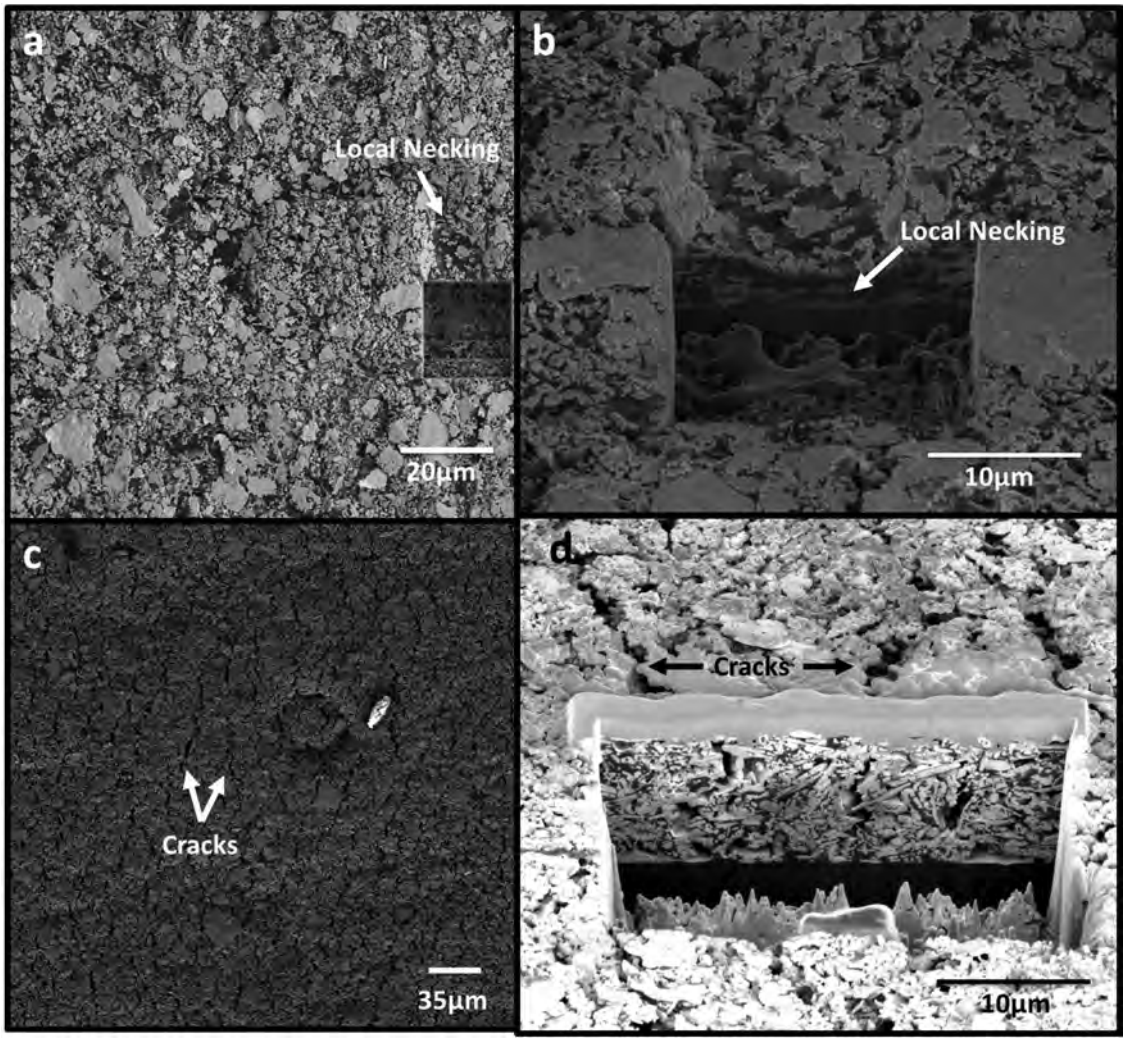

Fig. 6. Low-magnification top-down or inclined SEM images of both inks, post 35% strain: (a)–(b) Local necking in 5025 flexible ink (c) Surface cracking in PE874 stretchable ink (d) alignment of internal voids with surface cracks in PE874.

Both inks on PET have a linear increase with resistance up to 20% strain after which, the resistance for 5025 rapidly increases. PE874 performed much better than 5025 with applied strain. Fig. 4(b) plots the ratio of normalized resistance values between 5025 and PE874 when strained on PET. The disparity in electrical performance appears to increase linearly, such that by 35% applied strain the normalized resistance increase is 3 times more for 5025 than for PE874.

3.3. Strain Localization

Fig. 5(a) and (c) shows optical images of the surface of the two inks from 0 to 15% strain (see also the Supplementary Material section for a more complete set of images from 0 to 35% strain). PE 874 develops surface cracks that are visible starting ~5-7% applied strain, while 5025 exhibits no discernible changes in the optical images with applied strain. The cracks for PE874 are broadly distributed throughout the image, which suggests a universal response in this ink.

Fig. 5(b) and (d) shows the in-plane strain along the stretch direction (ε_{xx}) up to 15% applied strain. Color bar scaling is set from 0-100% strain. In both cases, we see that strain localizes in narrow bands that are initially oriented perpendicular to the direction of applied strain. For 5025, the localization begins at low applied strain levels. At 7% applied strain, the strain within the localization bands is 4 times greater than the applied strain for 5025 and 3 times greater than the applied strain for PE874. The strain in between the bands is much lower and some regions within the bands can remain undeformed (have zero strain). The very low levels of strain are within the resolution limit of the current optical imaging setup and the pattern used e.g. the natural contrast between flakes and binder. We also note that the strain within the localization bands can be even greater than a factor of 3 or 4 from the applied strain since the in-plane "local" strain is averaged over the subset window size and strain window size. The spacing of the localization bands is periodic and two-dimensional Fourier transformation of the strain field was used to identify the band spacing to be 28 μm for 5025, and 32 μm for PE874. Moreover, as the applied strain increases beyond 10%, the individual localization bands begin to also combine along the lateral direction.

As the bands interconnect, above 15% applied strain, the integrity of distinct localization bands breaks down, especially for 5025 so that more areas of the ink are involved in accommodating the macroscopic applied strain resulting in a more even distribution of the field. Strain is therefore accommodated in more regions, contributing to largely uniform reduction in thickness for 5025. Since PE874 exhibited surface cracking, Poisson effects are superseded and significant thickness reduction is not expected, as shown next.

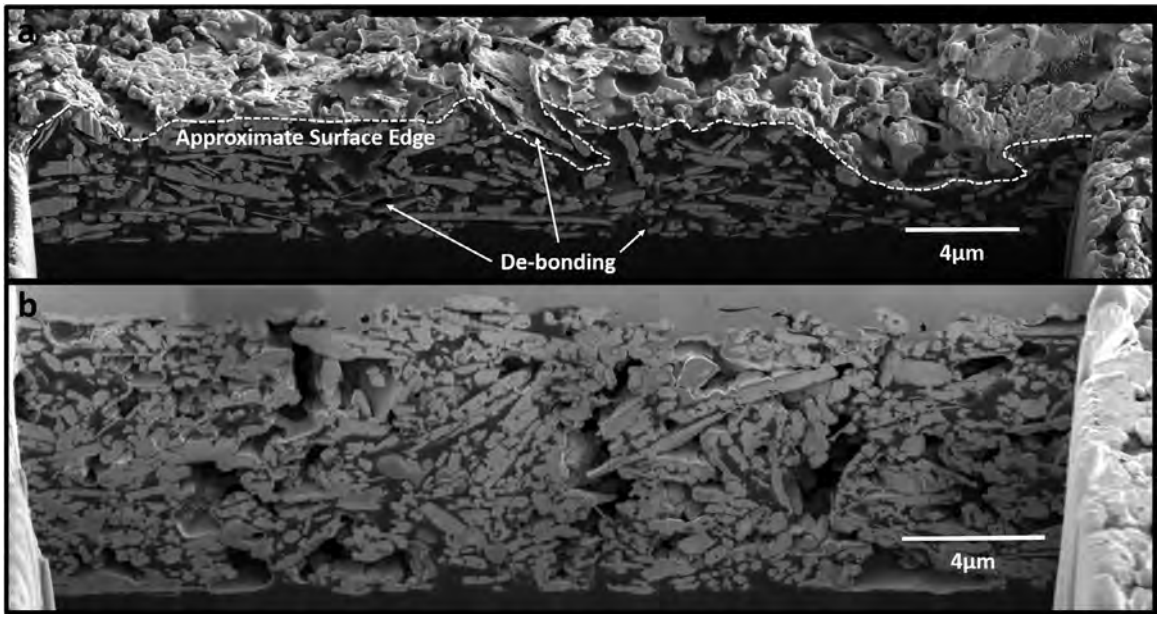

Fig. 7. SEM cross-sectioned areas of both inks, post 35% strain: (a) flake-matrix debonding and extreme thickness reduction (see right end of cross-section) in 5025 flexible ink (b) expanded and oriented internal voids in PE874 stretchable ink

3.4. Fractography

Given that far-field applied strain is largely accommodated through localized band formation for both inks, SEM images of post-test plan and through thickness cross-sections (after tests to 35% applied strain) were taken to further understand the differences in damage behavior between the two inks. Fig. 6(a) and (c) shows the plane-view surfaces for each ink after 35% strain. There are marked differences from the initial SEM top view images of Fig. 3. In 5025, significant debonding between silver flakes and the matrix (that can be better seen on Fig. 7(a)) have occurred. Moreover, some regions have undergone extreme reductions in ink thickness (see Fig. 6(b)) that appear to also have a lower flake density compared to surrounding ink space. For PE874 cracks are present throughout the area, with spacing of approximately 30 μm that coincides with the initial localization spacing identified from the strain maps (see Fig. 5).

Fig. 7 shows two cross-sections of 5025 and PE874. For 5025 the same flake-matrix debonding observed at the surface is seen within its thickness. The overall ink thickness decreased to approximately 4–6 μm, however within the local necking areas, thickness decreased to as low as 2 μm (see Fig. 7(a)). In contrast, in PE 874 the thickness only decreased to approximately 10 μm, with no local necking. Of particular note is the apparent coalescence and growth of voids within this ink. Orientation and spacing of expanded voids coincide with that of the surface cracks observed (see Fig. 6(d)). To summarize, the fractography results highlight that significant plastic deformation occurs with 5025, resulting in large thickness reductionespecially within local necking areas. These large plastic deformations are consistent with the widespread debonding observed between flakes and matrix. In contrast, the widespread cracks observed with PE874 have little plastic deformation in their vicinity, as evidenced by the small thickness reduction in these areas. Instead, damage/deformation is localized within these cracks. For the two inks, there is therefore a difference in flake distributions and thicknesses that should impact electrical resistance increases differently.

Figs. 8 and 9 compare the height and flake fraction distribution plots obtained from the binarized cross-sections shown in Figs. 3 and 7, for 5025 and PE874, respectively. The flake fraction along the cross-section length was calculated and normal distribution curves were fit to the data. For 5025, the flake fraction average changes from 49% to 35% after straining. Within the local necking regions of the ink, this fraction averages about 25%. This is significant, in that both the thickness and flake fraction are known to negatively impact the resistance in these local areas. PE874, exhibits minimal changes to thickness and maintains its mean flake fraction value of 54.5%, with a slightly higher standard deviation of 11%. But void fraction increases to 24.7%, a 45% increase compared to the initial 17% void fraction. It is important to note that these voids do not appear to cover the full through-thickness of the ink, however their vertical height is extensive. As such, while there are no significant reductions in overall ink thickness with PE874, the effective local thickness is reduced after the appearance of the surface cracks. Within the cross section captured, an area below a grouping of voids measures 1.4 μm in height, comparable to that of 5025. However, mean flake fraction in this area is significantly higher, at 42%.

4. Discussion

Connecting the observed increase in resistance with the relevant underlying physics is necessary to provide insight, and for enabling future material improvements. For such inks, the electrical conductivity of a percolating network of silver flakes can be related to applied strain that also causes the sample volume to initially increase, due to Poisson's effect [41]. The increase in the sample volume is mainly due to the increase in volume of the polymer matrix, which leads to a decrease in the silver flake fraction and, subsequently, a decrease in the electrical conductivity. Therefore, such percolation models show that as the strain increases, the conductivity decreases, and the resistance increases. For such models, the spatial distribution of filler material was assumed to be uniform [41]. Ergo strain distribution is uniform, *i.e.*, there is no strain localization. To describe this affine transformation, the expression for the electrical conductivity according to Mamunya [41] is:

$$\frac{\sigma}{\sigma_c} = 1 + \left(\frac{\sigma_m}{\sigma_c} - 1\right)\left[\frac{\varphi - \varphi_c}{\varphi_{max} - \varphi_c}\right]^s \tag{2}$$

where, σ is the conductivity of the composite, σ_c is the conductivity of the composite at the percolation threshold, σ_m is the conductivity of the metal, ϕ is the silver flake fraction, ϕ_c is the flake fraction defining the percolation threshold, ϕ_{max} is the maximum flake fraction, and s is the power law exponent. The change in the flake fraction of a sample subject

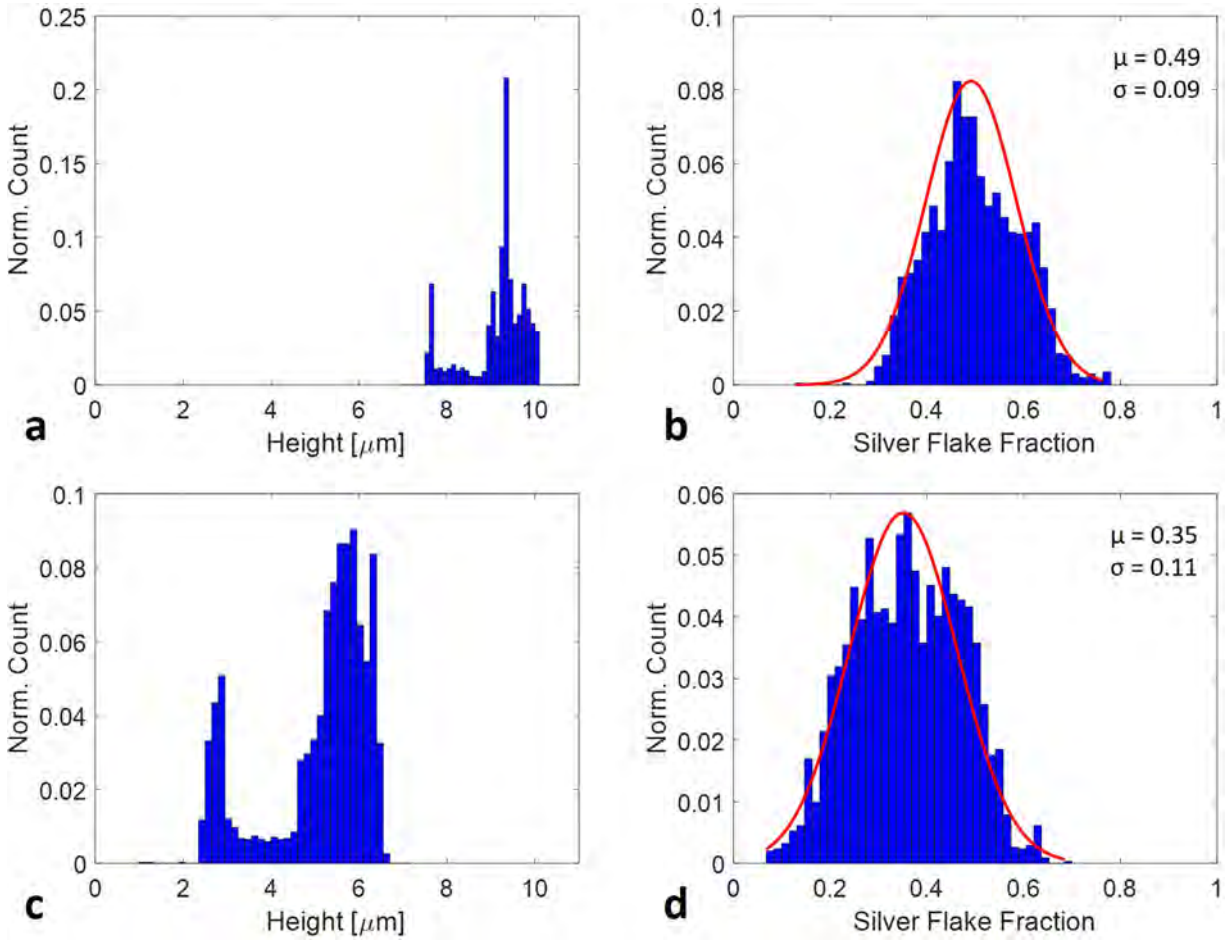

Fig. 8. 5025 flexible ink height and flake fraction: (a) height distribution, unstrained (b) flake fraction, unstrained (c) height distribution, post 35% strain (d) flake fraction, post 35% strain.

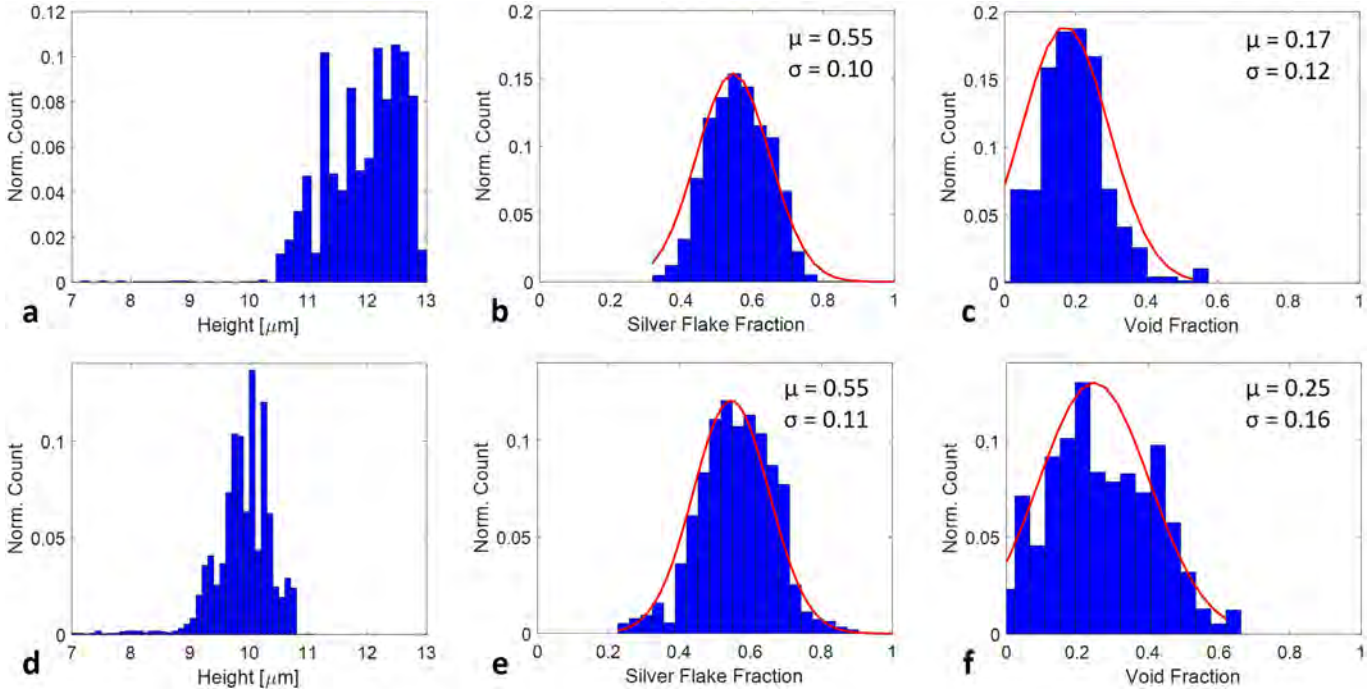

Fig. 9. PE874 stretchable ink height, flake, and void fraction: (a) height distribution, unstrained (b) flake fraction, unstrained (c) void distribution, unstrained (d) height distribution, post 35% strain (e) flake fraction, post 35% strain (f) void fraction, post 35% strain.

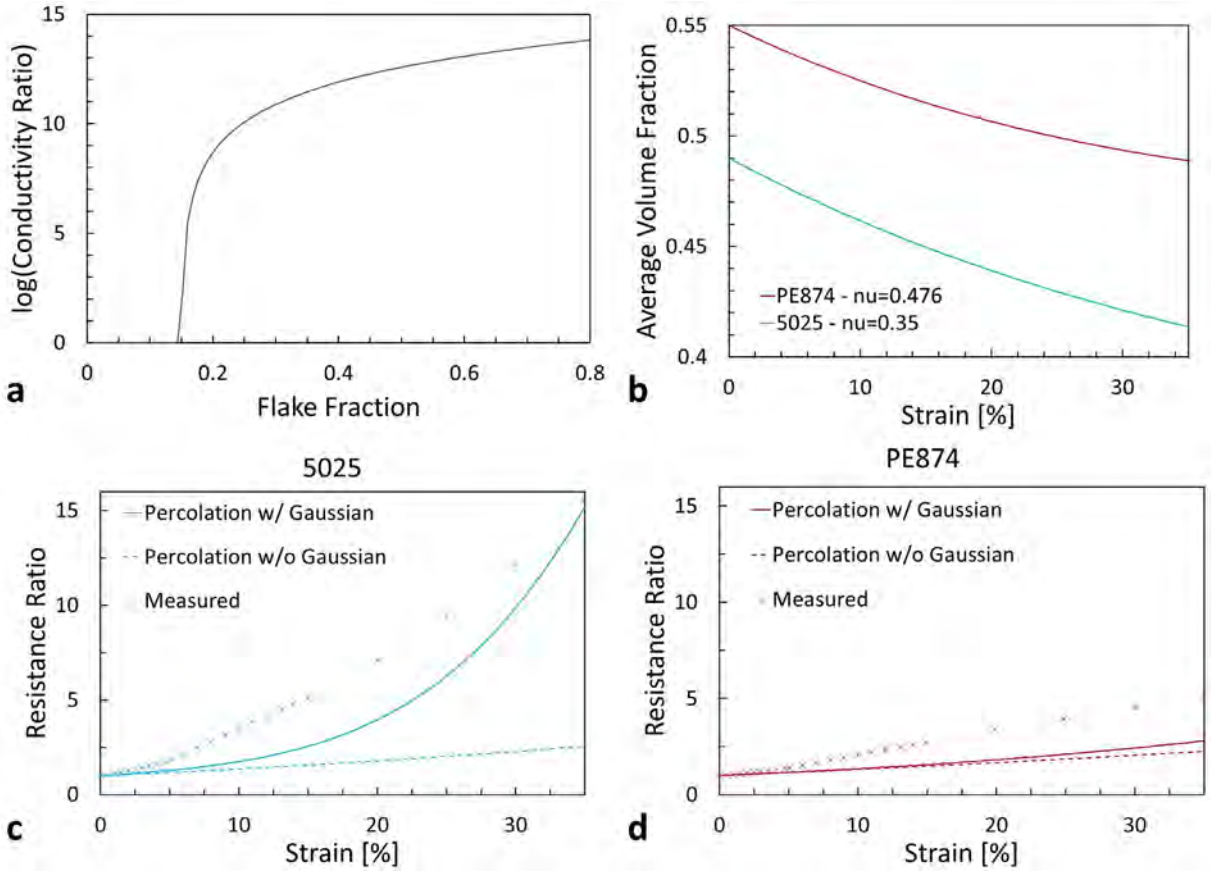

Fig. 10. Numerical model predictions: (a) conductivity (log scale) with increasing volume fraction for both inks (Eq. (2)) (b) average flake volume fraction with strain (Eq. (3)) (c) and (d) numerical model predictions of normalized resistance ratio vs. strain for 5025 and PE874, respectively.

to uniaxial strain is

$$\varphi(\varepsilon, \nu) = \frac{\varphi_0}{(1+\varepsilon)(1-\nu\varepsilon)} \tag{3}$$

where the denominator represents the increase in volume of the sample, ϕ_0 is the initial flake fraction, and ε is the strain. Eq. (3) accounts for shrinkage in only the thickness dimension (i.e. assuming no decrease in width as a simplification). Combining Eq. (2) and (3) gives the relative conductivity ratio as a function of strain, the inverse of which provided the resistivity ratio. When the line is stretched, the relationship between resistivity and resistance (see Eq. (1)) must also include the effect of strain on ink length, L and cross-sectional area, A:

$$R_\varepsilon = \frac{\rho_\varepsilon L(1+\varepsilon)}{A(1-\nu\varepsilon)} \tag{4}$$

The above relations are modified to include the effects of strain localization through inclusion of a spatial inhomogeneity of the flake fraction, as measured in Figs. 8 and 9. For the unloaded 5025, the flake fraction can be represented by a Gaussian distribution, with a mean of 49% and a standard deviation of 9%. After being strained to $\varepsilon = 0.35$, the flake fraction distribution shifted to a mean of 35 % with a standard deviation of 11%. The effect of an evolving flake distribution with strain can be obtained through modification of Eq. (2), where the conductivity along a printed line can be divided into a series of short segments, with the loading in each segment distributed in a Gaussian fashion. The origin of the disparate flake fraction areas may be the strain localization that creates segments that have low flake fraction, and low conductivity, which exacerbates the increase in resistance of the printed line as a whole.

The impact of the uniform vs. localized strain on the resistance is examined for the 5025 ink through an evolving vs. non-evolving silver flake fraction distribution. For both models, these are the parameters used for 5025:$\nu = 0.35$, $s = 2$, $\varphi_c = 0.13$, $\sigma_m/\sigma_c = 10^6$, and $\varphi_{max} = 0.8$ (see Fig. 10(a)). The ratio of the increase in resistance is very sensitive to factors like the percolation threshold, which is not known for the silver flakes used here. For spheres, the percolation threshold is $\varphi_c = 0.18$, but it will be lower than that for flake particles [41]. Under uniform strain the model, per Eq. (2), with an average loading expression predicts a 2.6 times increase in resistance at 35% strain for the 5025 ink, which is much lower than the observed increase in resistance. Under localized strain, modeled by allowing the local flake fraction to follow a Gaussian distribution, the resistance is predicted to increase by a factor of 15 at 35% strain, which is similar to the experimental value (see Fig. 10(c)). Clearly incorporation of a non-uniform loading, as a way of accounting for the strain localization impact, results in a much higher increase in the resistance of a printed line.

For the PE874 ink only the following parameters are different from those used for 5025: an initial volume loading of 55%, and $\nu = 0.476$. For a non-evolving flake fraction distribution, Eq. (2) predicts the resistance increase to be 2.3 times higher, not very different from the 2.6 resistance change for 5025. Incorporating the measured Gaussian distribution (see Fig 9(d)) did not result in any significant change (see Fig. 10(c)) (2.8 vs. original 2.3 at 35%) and does not wholly account for the experimental resistance ratio of 5 at 35%. The 5 times increase in resistance for PE 874 can be explained by recognizing the ink's resistance reduction is due to the appearance of surface cracks. When PE874 is stretched, the distribution of flake fraction did not change (see Fig. 9(b) and (e)), which is inconsistent with Eq. (3) predicting a decrease in flake fraction from 0.55 to 0.49 (see Fig. 10(b)). This is likely the result of cracking (see Fig. 6(d)), preventing deformation in adjacent areas, and therefore resulting in a constant flake fraction, and also leading to an increase in the void content (see Fig. 9(c) and (f)). The response of this ink may

be better modeled using porous metals where one phase is electrically conductive, but the void phase has no conductivity. It is known that the electrical conductivity of a metal decreases linearly with the introduction of pores at low porosity, with some curvature at higher values of porosity [32,33]. If all the volume increase in the PE874 is caused by an increase in void volume, then we would expect the electrical resistivity to increase linearly with the void volume, which matches the trend in the data.

5. Conclusions

In conclusion, this work highlighted the importance of the initial architecture of silver inks on the deformation and electrical behavior up to large strains (in excess of 30%). While the investigated 5025 and PE874 inks were expected to differ only in their polymer matrix properties, our FIB cross-sections revealed a large presence of micron-size voids in the PE874 inks. Our in-situ strain map analysis showed the formation of strain localization bands at early applied strain levels. These strain localization bands have different origins, which result in different flake volume fraction evolutions and therefore different electrical behavior. For PE874, strain localization is associated with cracking, most likely triggered by the pre-existing voids, which leads to minimal silver flake fraction changes and a resistance ratio increase of 5 at 35% applied strain. Instead, for 5025, strain localization is accompanied by local necking which leads to large flake fraction decreases and a resistance ratio increase of 15 at 35% applied strain. Percolation theory can provide reasonable estimates of the resistance ratio increase with strain for 5025 if the Gaussian distribution representing the measured flake fraction (which captures non-uniform deformation) is used, compared to the use of average flake fraction (which better captures uniform deformation).

This work suggests the somewhat paradoxical conclusion that voids, which lead to cracks in the deformed inks, can be beneficial for their electrical behavior under large strains. Indeed, while presence of surface cracks means an increase in void fraction, and therefore an increase in resistance (increase in porosity), their formation prevents any significant decrease in flake fraction (especially in necked regions). Since these are only surface and not through-thickness cracks, their formation appears to be not as detrimental to the ink's overall electrical behavior. Investigating PE874 inks with different initial void contents (presumably by optimizing the fabrication process) would be useful to further understand the combined effect of voids and strain localization on electrical behavior under large strains.

Declaration of Competing Interest

The authors declare that they have no known competing financial interests or personal relationships that could have appeared to influence the work reported in this paper.

Acknowledgments

The authors acknowledge Nextflex for funding this research. Further acknowledgements are extended to Lynne Dellis and Michael Creamer at DuPont, whose extensive knowledge and experience ensured reliability and repeatability in printing of these samples using controlled proprietary processes.

Supplementary materials

Supplementary material associated with this article can be found, in the online version, at doi:10.1016/j.mtla.2020.100642.

References

[1] J. Kim, et al., Epidermal electronics with advanced capabilities in near-field communication, Small 11 (8) (2015) 906–912.
[2] Y. Liu, et al., Flexible, stretchable sensors for wearable health monitoring: sensing mechanisms, materials, fabrication strategies and features, Sensors 18 (2) (2018) 645.
[3] D. Briand, et al., Making environmental sensors on plastic foil, Mater. Today 14 (9) (2011) 416–423.
[4] F.-R. Fan, Z.-Q. Tian, Z. Lin Wang, Flexible triboelectric generator, Nano Energy 1 (2) (2012) 328–334.
[5] M.F. El-Kady, R.B. Kaner, Scalable fabrication of high-power graphene micro-supercapacitors for flexible and on-chip energy storage, Nat. Commun. 4 (2013) 1475.
[6] W.T. Dang, et al., Printable stretchable interconnects, Flex. Printed Electron. 2 (1) (2017).
[7] D. McCoul, et al., Recent advances in stretchable and transparent electronic materials, Adv. Electron. Mater. 2 (5) (2016).
[8] S. Yao, Y. Zhu, Nanomaterial-enabled stretchable conductors: strategies, materials and devices, Adv. Mater. 27 (9) (2015) 1480–1511.
[9] A.R. Rathmell, B.J. Wiley, The synthesis and coating of long, thin copper nanowires to make flexible, transparent conducting films on plastic substrates, Adv. Mater. 23 (41) (2011) 4798–4803.
[10] S. De, et al., Silver nanowire networks as flexible, transparent, conducting films: extremely high DC to optical conductivity ratios, ACS Nano 3 (7) (2009) 1767–1774.
[11] F. Carpi, et al., Electromechanical characterisation of dielectric elastomer planar actuators: comparative evaluation of different electrode materials and different counterloads, Sens. Actuators A – Phys. 107 (1) (2003) 85–95.
[12] C.K. Gong, et al., A healable, semitransparent silver nanowire-polymer composite conductor, Adv. Mater. 25 (30) (2013) 4186–4191.
[13] S. Yun, et al., Compliant silver nanowire-polymer composite electrodes for bistable large strain actuation, Adv. Mater. 24 (10) (2012) 1321–1327.
[14] T.A. Kim, et al., Single-walled carbon nanotube/silicone rubber composites for compliant electrodes, Carbon 50 (2) (2012) 444–449.
[15] F. Xu, et al., Wavy ribbons of carbon nanotubes for stretchable conductors, Adv. Funct. Mater. 22 (6) (2012) 1279–1283.
[16] F. Xu, Y. Zhu, Highly conductive and stretchable silver nanowire conductors, Adv. Mater. 24 (37) (2012) 5117–5122.
[17] S. Yao, Y. Zhu, Wearable multifunctional sensors using printed stretchable conductors made of silver nanowires, Nanoscale 6 (4) (2014) 2345–2352.
[18] C. Katsarelis, et al., Crack initiation of printed lines predicted with digital image correlation, Jom 70 (9) (2018) 1805–1810.
[19] A. Wyss, et al., Monitoring of stress-strain evolution in thin films by reflection anisotropy spectroscopy and synchrotron X-ray diffraction, J. Mater. Sci. 52 (11) (2017) 6741–6753.
[20] O. Glushko, et al., Monotonic and cyclic mechanical reliability of metallization lines on polymer substrates, J. Mater. Res. 32 (9) (2017) 1760–1769.
[21] B.J. Kim, et al., Effect of film thickness on the stretchability and fatigue resistance of Cu films on polymer substrates, J. Mater. Res. 29 (23) (2014) 2827–2834.
[22] B.J. Kim, et al., Improving mechanical fatigue resistance by optimizing the nanoporous structure of inkjet-printed Ag electrodes for flexible devices, Nanotechnology 25 (12) (2014) 6.
[23] N. Lambricht, T. Pardoen, S. Yunus, Giant stretchability of thin gold films on rough elastomeric substrates, Acta Mater. 61 (2) (2013) 540–547.
[24] G.D. Sim, et al., Improving the stretchability of as-deposited Ag coatings on poly-ethylene-terephthalate substrates through use of an acrylic primer, J. Appl. Phys. 109 (7) (2011) 5.
[25] N.S. Lu, Z.G. Suo, J.J. Vlassak, The effect of film thickness on the failure strain of polymer-supported metal films, Acta Mater. 58 (5) (2010) 1679–1687.
[26] N.S. Lu, et al., Failure by simultaneous grain growth, strain localization, and interface debonding in metal films on polymer substrates, J. Mater. Res. 24 (2) (2009) 379–385.
[27] N.S. Lu, et al., Metal films on polymer substrates stretched beyond 50%, Appl. Phys. Lett. 91 (22) (2007) 3.
[28] Ibru, T., et al., Stress-induced surface instabilities and defects in thin films sputter deposited on compliant substrates. 2017. 13(22): p. 4035–4046.
[29] M. Vosgueritchian, D.J. Lipomi, Z.A. Bao, Highly conductive and transparent PEDOT:PSS films with a fluorosurfactant for stretchable and flexible transparent electrodes, Adv. Funct. Mater. 22 (2) (2012) 421–428.
[30] Y.H. Kim, et al., Highly conductive PEDOT:PSS electrode with optimized solvent and thermal post-treatment for ITO-free organic solar cells, Adv. Funct. Mater. 21 (6) (2011) 1076–1081.
[31] T.S. Hansen, et al., Highly stretchable and conductive polymer material made from poly (3,4-ethylenedioxythiophene) and polyurethane elastomers, Adv. Funct. Mater. 17 (16) (2007) 3069–3073.
[32] H. Boys, et al., A dielectric elastomer actuator-based tactile display for multiple fingertip interaction with virtual soft bodies, Electroact. Polym. Actuators Dev. (Eapad) 2017 (2017) 10163.
[33] M. Matysek, et al., Dielectric elastomer actuators for tactile displays., in: Proceedings World Haptics 2009: Third Joint Eurohaptics Conference and Symposium on Haptic Interfaces for Virtual Environment and Teleoperator Systems, 2009, pp. 290–295.
[34] W. Yuan, et al., New electrode materials for dielectric elastomer actuators, Electroact. Polym. Actuators. Dev. (Eapad) 2007 (2007) 6524.
[35] A.P. Robinson, et al., Microstructured silicone substrate for printable and stretchable metallic films, Langmuir 27 (8) (2011) 4279–4284.
[36] J. Jones, et al., Stretchable wavy metal interconnects, J. Vac. Sci. Technol. A 22 (4) (2004) 1723–1725.

[37] X.L. Wang, et al., Stretchable conductors with ultrahigh tensile strain and stable metallic conductance enabled by prestrained polyelectrolyte nanoplatforms, Adv. Mater. 23 (27) (2011) p. 3090-+.
[38] J.J. Liang, et al., Silver nanowire percolation network soldered with graphene oxide at room temperature and its application for fully stretchable polymer light-emitting diodes, ACS Nano 8 (2) (2014) 1590–1600.
[39] P. Lee, et al., Highly stretchable or transparent conductor fabrication by a hierarchical multiscale hybrid nanocomposite, Adv. Funct. Mater. 24 (36) (2014) 5671–5678.
[40] K.Y. Chun, et al., Highly conductive, printable and stretchable composite films of carbon nanotubes and silver, Nat. Nanotechnol. 5 (12) (2010) 853–857.
[41] Y.P. Mamunya, et al., Electrical and thermal conductivity of polymers filled with metal powders, Eur. Polym. J. 38 (9) (2002) 1887–1897.
[42] Y. Kim, et al., Stretchable nanoparticle conductors with self-organized conductive pathways, Nature 500 (2013) 59.
[43] M.J. Cordill, J. Berger, T. Jörg, 33-2: invited paper: evaluating reliability of flexible electronic materials with combined electro-mechanical testing techniques, SID Sympos. Dig. Techn. Pap. 47 (1) (2016) 415–418.
[44] Scientific, L. TST350 temperature controlled tensile stress testing stage: user guide. Available from: https://static1.squarespace.com/static/556d800ae4b0e8f91507450c/t/56cf394886db43237cbed222/1456421216282/TST350_T95_manual.pdf.
[45] J. Blaber, B. Adair, A. Antoniou, Ncorr: open-source 2D digital image correlation Matlab software, Exp. Mech. 55 (6) (2015) 1105–1122.
[46] National Institute of Health, U. ImageJ. Image J, Image Processing and Analysis in Java [1.51j8].